Vibration Test Method to Study Elastic Stability of Porous Carbon Nanocomposite Counter Electrode in Dye Sensitized Solar Cells

Wei Zeng,[†,‡] Guojia Fang,*,[†] Borui Li,[†] Zhiqiang Liu,[‡] Tianyang Han,[†] Jing Wang,[†] Fuwei Liu,[†] Pengfei Fang,[†] Xingzhong Zhao,[†] and Dechun Zou[§]

[†]Key Laboratory of Artificial Micro- and Nano-structures of Ministry of Education of China, School of Physics and Technology, Wuhan University, Wuhan, 430072, P. R. China

[‡]College of Science, Jiujiang University, Jiujiang, 332005, P. R. China

[§]Beijing National Laboratory for Molecular Sciences, Key Laboratory of Polymer Chemistry and Physics of the Ministry of Education, College of Chemistry and Molecular Engineering, Peking University, Beijing 100871, P. R. China

ABSTRACT: An out-of-plane elastic vibration test method is developed to directly study the elastic stability of elastic Ti foil-supported porous carbon nanocomposite (CNC) counter electrode (CE) of dye sensitized solar cells (DSSCs). The stability of CE, estimated by that of power conversion efficiency (PCE) of the CE-based DSSC device, is studied from the views of CNC morphology, equivalent resistances, exchange current density and contact model of CE. The results suggest thinner thickness and bigger interbundling degree of CNC layer is beneficial to the total internal impedance value of CE, and then beneficial to the CE stability. With optimal CNC structure, even if the CE is springed 1000 times with max amplification about 10 mm, the PCE of CE-based DSSC can remain 80% of the initial value. The test method is interesting and the results may have a potential use for elastic stability study of general elastic devices.

KEYWORDS: vibration, elastic stability, carbon nanocomposite, counter electrode, dye sensitized solar cells, contact model
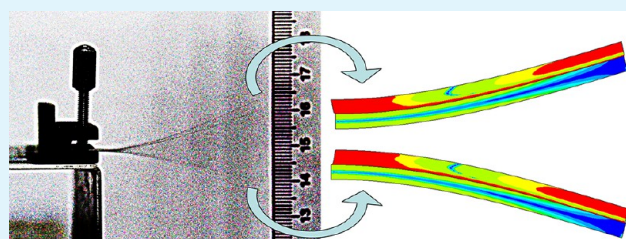
1. INTRODUCTION

Elasticity is a physical property of materials, which can return to their original shape after they are deformed. Elastic material is not only bendable but also can self-recover deformation after being bent. Nowadays, bendable materials have been considered as important components in future electronic devices including piezoelectricity,[1] skinlike sensor,[2,3] paperlike displayer,[4] and flexible solar cells.[5] Compared to general bendability, elasticity can endow material additional force functions, such as supporting,[6,7] buffering,[8] and vibration.[9,10] These can further enlarge the application domains for bendable materials.

Performance stability is always an important evaluation index for elastic devices. In most elastic devices, elastic electrodes are inevitable. They are generally composed of a functional layer and elastic substrate. The performance stability of upper functional layer is always challenging, especially when it is a porous and fragile inorganics.[11] In order to solve this problem, interweaving additives, such as polymers,[12−14] metals,[15,16] and carbon nanomaterials,[17,18] are suggested to add into the layer to reinforce the materials. In addition, a adhesion layer is proposed to insert the interface between the functional layer and substrate.[19] Theoretical studies such as Euler−Bernoulli theory,[20] and Timoshenko beam theory[21,22] are carried out. Three main failure modes of cracking, slipping and delamination are suggested.[23] So far, most stability studies employ bend test method, i.e., simplex inward or outward bend.

However, vibration is the realistic movement mode for elastomer. The vibration is alternately inward and outward bend. In vibration, the upper functional materials in high vibration frequency are easily separated from the substrate and then flicked out. Therefore, the vibration is different to the common bend. A direct vibration test more approaches to the realistic movement mode of elastomer, so it is more suitable for elastic stability study. To this day, the research in this method is rarely reported to our knowledge.

In this paper, an out-of-plane vibration test method is carried out to study the elastic stability of counter electrode (CE) in dye-sensitized solar cells (DSSCs). The CE is composed of carbon nanocomposite (CNC) functional layer and elastic Ti foil substrate. The performance stability of CE is estimated by the stability of power conversion efficiency (PCE) of the CE-based DSSC device. The stability is studied from the views of CNC morphology, equivalent resistances, and exchange current density of CE. Moreover, elastic strain and deformation of CE are studied by a contact model. The results suggest that the stability of total internal impedance of CE (R_{SUM}) can effectively reflect the stability of CE. Thinner thickness and bigger interbundling degree of CNC layer are beneficial to R_{SUM} stability, and then beneficial to PCE stability. With

optimal CNC structure, even if the CE is springed 1000 times with a max amplification about 10 mm, its R_{SUM} value varies less than 10% and PCE of the cell can remain 80% of the initial value. The test method is interesting and the results have potential use for elastic stability study in general elastic devices.

2. EXPERIMENTAL SECTION

Preparation of CNC CE. A flat Ti foil (purity: 99.7%) of 0.2 mm thickness was used as CE substrate. For all CEs, the substrates have the same sizes of 5.5 cm × 1 cm. After the substrate was cleaned, a layer of Ni film was electrically deposited on the substrate. Next, the substrate was rinsed in hot water and then in ethanol so as to remove residual plating solution. After inartificially dried, the substrate was combusted in an ethanol flame for 5 min. To avoid the moisture effect, we stashed the generated CNC CEs in an ultra−low humidity storage cabinet before vibration test. In the cabinet, the temperature is about 25 °C and relative humidity is about 5%. The detailed electrical deposition conditions are listed in Table 1. The detailed processes of Ti substrate pretreatment and frame synthesis are described elsewhere.[24,25]

Table 1. Electrical Deposition Conditions for Ni Layer

composition or parameter	data
nickel sulfate ($NiSO_4 \cdot 6H_2O$)	1.00 M
nickel chloride ($NiCl_2$)	0.20 M
boric acid (H_3BO_3)	0.65 M
lauryl sodium sulfate	0.24 mM
pH value	3
voltage	1.00 V
bath temperature	70 °C

Preparation of Photoanodes. The fabrication procedures for photoanodes were the same as those in our previous work.[24] In brief, a fluorine-doped tin oxide (FTO, about 14 Ω/ sq) conductive glass was used as substrate. Then, a compact TiO_2 film about 50 nm and porous TiO_2 film about 14 μm were coated on the substrate in sequence. The dye sensitizer was N719.

Assembling and Test. The morphology analysis were carried out by a scanning electron microscopy (SEM, JEOL 6700F, Japan). Electrochemical impedance spectroscopy (EIS) and Tafel polarization curves were measured with symmetrical dummy cells. The identical CEs were separated by a Teflon film of 100 μm thickness. The electrolyte contains 1 M 1-methyl-3-propyl imidazolium iodide, 0.04 M LiI, 0.03 M I_2, 0.1 M guanidinium thiocyanate, and 0.5 M 4-tert-butylpyridine in a solution of acetonitrile and propylene carbonate (v:v = 1:1).[26] The irradiated area of cells was kept as 0.25 cm^2. The EIS measurements were performed with a frequency ranging from 100 kHz to 0.1 Hz at zero bias potential.

The photocurrent density−voltage (J−V) characteristics were recorded by a standard ABET Sun 2000 Solar Simulator under 100 mW cm^{-2}, with AM 1.5 simulated irradiation. The J−V, EIS, and Tafel measures were collected using a CHI 660D electrochemical workstation (Shanghai, China). The electrolyte for J−V measurement is the same as that for EIS and Tafel measurements.

Elastic test is performed with homemade equipment as shown in Figure 1a. The test samples are those unpruned Ti-foil-supported CNC CEs. They have the same shapes and sizes to ensure effective performance comparison. In test, the CNC side of CE is upward. A schematic diagram of function declaration for a test CE is shown in Figure 2. The left region is for fixation with a metallic supporter as shown in Figure 1a. The right region is for downward press to generate vibration. The CNC on the two end regions are easily to be damaged artificially, so the CNCs are not grown intentionally on those regions. Therefore, as shown in Figure 2, just the middle region about 10 mm width (W) grown with CNC is chosen for research. In the following sections, the samples for all characterizations are acquired on this research region. To arouse vibration, we downward-pressed the electrode on the press region manually, as shown in Figure 1b. The
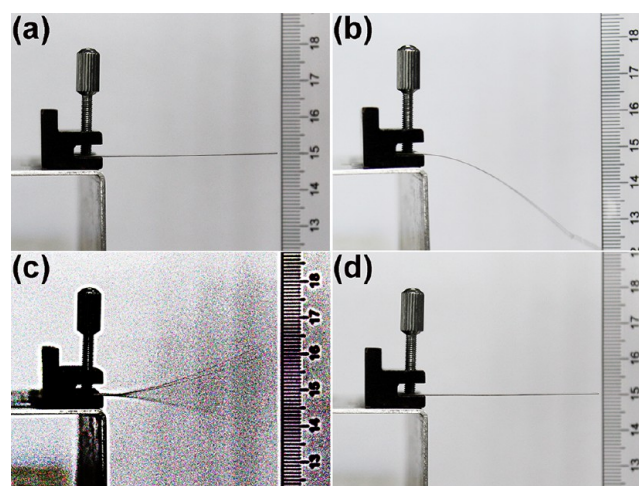

Figure 1. Vibration test equipment and electrode statuses in vibration test process. (a) Vibration test equipment and the initial electrode status before vibration. (b) Electrode status under downward pressure. (c) Vibration status in high vibration frequency. (d) Final status after vibration.
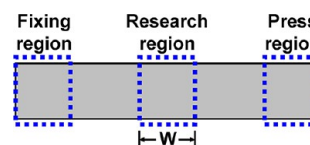

Figure 2. Schematic diagram for exhibiting the role of different regions on a CE in vibration test.

downward displacement of the right end is about 20 mm, the value of which is chosen for arousing an elastic vibration with vibration amplitude as large as possible. Therefore, for the CNC on middle research region, the real vibration amplitude is just about 10 mm. When the pressure is released, the vibration status with high vibration frequency is shown in Figure 1c. In about 5 s, the electrode restores to its initial shape, as shown in Figure 1d. For clear expression, an entire test process shown from Figure 1a−d is defined as a vibration cycle, and 200 times of vibration cycles is defined as one vibration section. Each section test needs about 1 h, so the needed time for continuous 5 sections is less than 6 h. The vibration test is carried out in a closed lab. The environment temperature is about 25 °C and relative humidity is about 50%.

3. SIMULATION SECTION

The CNC CE is modeled with a two-dimensional contact model in a finite element method. The model diagram is shown in Figure 3. The lower rectangle represents Ti substrate. Its
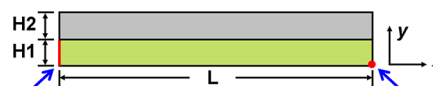

Figure 3. Schematic diagram of contact model for simulation.

width and height are L = 10 mm and $H1$ = 0.5 mm, respectively. The Young's modulus of Ti substrate in X and Y axis directions are both set of 1.02×10^{11} Pa. The Poisson's ratio is set as 0.3. The upper rectangle represents CNC layer. Its width is set the same as the substrate and its height is set of $H2$ = 0.5 mm. The Young's modulus of CNC layer in the Y axis direction (E_Y) is set of 1×10^2 Pa, and that in the X axis direction (E_X) is adjustable. The Poisson's ratio is 0.1. The
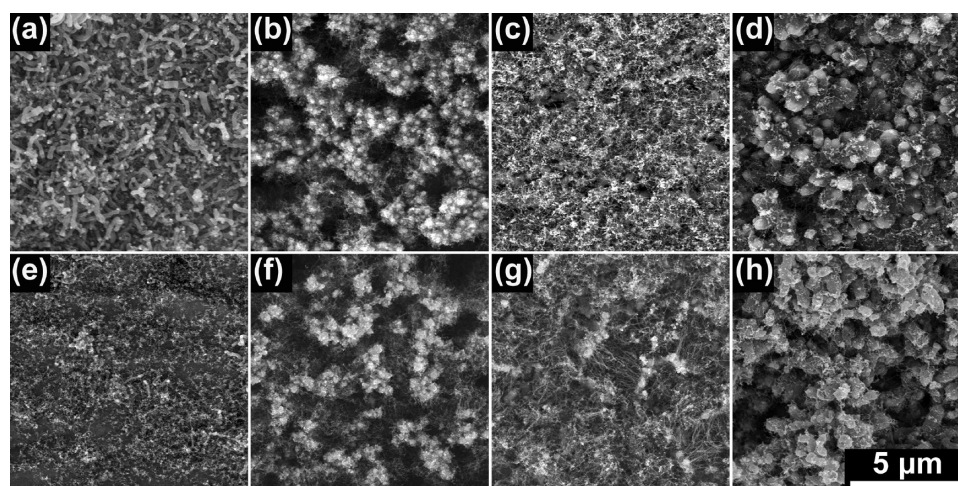
Figure 4. SEM images of CNCs on CEs in top view before and after five vibration sections. CE1: (a) before vibration, (e) after vibration. CE2: (b) before vibration, (f) after vibration. CE3: (c) before vibration, (g) after vibration. CE4: (d) before vibration, (h) after vibration. The scale bar in h applies to all images.
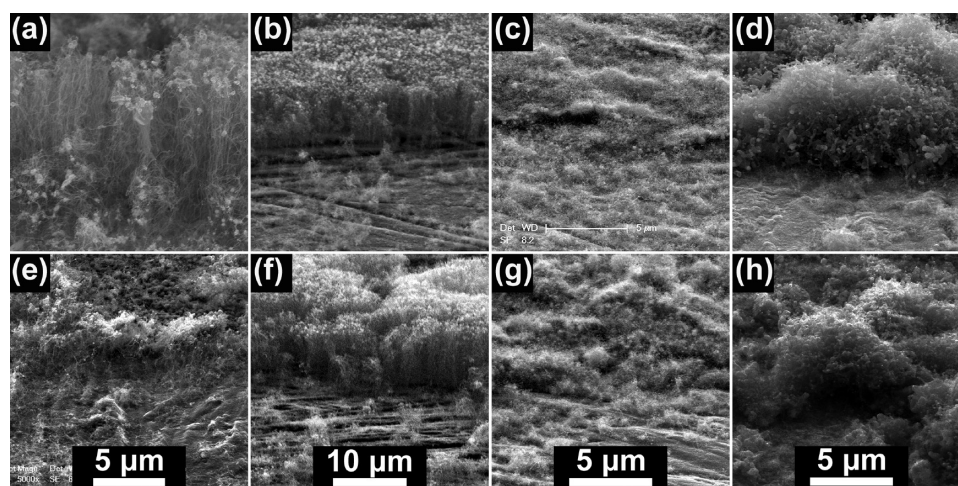

Figure 5. SEM images of CNCs on CEs in oblique view before and after five vibration sections. CE1: (a) before vibration, (e) after vibration. CE2: (b) before vibration, (f) after vibration. CE3: (c) before vibration, (g) after vibration. CE4: (d) before vibration, (h) after vibration. Each CE before and after vibration has the same scale bar shown in the after-vibration image.

shear modulus of CNC layer is set of 1×10^{-3} Pa. The friction coefficient at the interface between the two layers is set of 0.1. To simulate the fixing effect of left end on Ti substrate, we loaded a zero displacement on the left boundary of lower rectangle. The boundary is marked in red. To simulate the effect of maximum vibration amplification of right end on Ti substrate, a 2 mm displacement along the direction of Y axis is loaded on the bottom right keypoint of lower rectangle. The keypoint is marked in red.

4. RESULTS AND DISCUSSION

Morphology Variation. To study the effect of functional layer structure on elastic stability of CE, four elastic Ti-foil-supported CNC CEs are fabricated with different structures of CNC layers. Their structures are attributed to the thicknesses of precoated Ni catalyst layers. With Ni layer thickness about 33, 66, 130, and 780 nm, four CNC CEs are fabricated and signed as CE1, CE2, CE3, and CE4, respectively. Before and after five vibration sections, their morphologies are visualized by SEM in top and oblique views. Before being vibrated, the CE1 shows typical morphology of carbon nanotube (CNT)

(Figure 4a).[27] Other CNCs show hybridized structures with different hybridized degrees of CNT and particles (Figure 4b–d). These particles mainly are Ni particles, which come from the residual Ni catalytic agent when they are excessive.[24,28] In oblique view (Figure 5a–d), the CNC thicknesses on CE1, CE2, CE3, and CE4 are measured to be about 10, 10, 0.2, and 5 μm, respectively. With increasing Ni layer thickness, the CNC thickness first decreases from CE2 to CE3 (Figure 5b, c), and then increases to CE4 (Figure 5d). The thickness variation will be discussed in the following section of CNC growth mechanism. In panels a and b in Figure 5, the CNTs on CE1 and CE2 are mainly vertical to the substrate. Only weak horizontal interbundling phenomenon is observed. Compared to CE1 and CE2, the CE3 and CE4 (Figure 5c, d) show bigger horizontal interbundling degree, because the excessive residual Ni interbundles the CNTs. Similar interbundling effects have been reported in the literatures.[29,30] In addition, the horizontal interbundling is observed more obvious than vertical interbundling for these CEs. The interbundling is a key effect factor to elastic stability, which will be further discussed in the following sections.

The surface morphologies after the CEs are vibrated in five sections are shown in Figure 4e−h, and side morphologies are shown in images e−f in Figure 5. Comparison of the surface morphologies for each CE before and after five vibration sections is made. The difference for CE1 is most remarkable. The CNTs obviously turn sparser (Figure 4e). The morphology variations for these CEs are clearer in oblique views. After five vibration sections, few CNTs survive on CE1 (Figure 5e), slight cracks appear on CE2 (Figure 5f), and delamination is observed on CE3 and CE4 (Figure 5g, h).

For the upper functional layer, the thickness and Young's modulus are suggested two determining factors on the film bend stability.[23] With increasing thickness and unchanged Young's modulus of the functional layer, the failure mode of functional layer is demonstrated to evolve from crack, slipping to delamination in sequence.[23] However, here although the thickness of CNC film decreases from CE2 to CE3 (or CE4), the failure mode still evolves from crack to delamination. Therefore, the other determining factor, i.e., Young's modulus value of the functional layer, must have played a key role.

CNC Growth Mechanism. When the Ni layer thickness is 33 nm for CE1 or 66 nm for CE2, the generated CNTs are both about 10 μm thickness and almost aligned. The thin Ni layer offers high activity for CNT growth.[31] Their almost aligned structures are formed by the crowding effect of generated amount CNTs.[25,32] When the Ni layer thickness increases to 130 nm for CE3, the CNC products decrease to only 0.2 μm thickness. For CE3, growth process diagrams are deduced and shown in Figure 6a−c. Before combusted, the Ni-
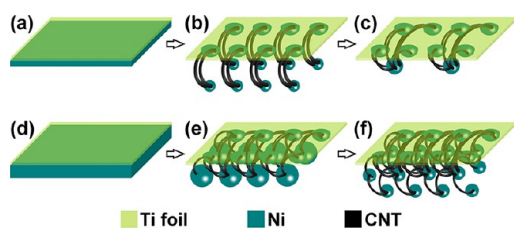

Figure 6. Growth mechanisms of CNCs on CE3 and CE4. (a−c) For CE3. (d−f) For CE4.

coated Ti foil is shown in Figure 6a, where the Ni layer side is facing to the ethanol flame. Because the Ni layer is thick, few

CNTs can be produced. Then, the excessive Ni components will melt and flow to the top of CNTs under the action of gravity, as shown in the Figure 6b. The sparse CNTs can not retain aligned and finally they fallen down. Then, the top Ni components melt together to make CNTs interbundled, as shown in Figure 6c. These can explain why the CNC layer on CE3 is thinner and interbundling.

When the Ni layer thickness increases to 780 nm for CE4, the CNC products increase to 5 μm thickness. For CE4, growth process diagrams are deduced and shown in Figure 6d−f. As shown in Figure 6d, the coated Ni is very thick, so the residual Ni components are abundant on the surface of interbundling CNC products, as shown in Figure 6e. On the basis of these top Ni components, more interbundling CNC can be further produced layer by layer, as shown in Figure 6f. Therefore, the CNC layer on CE4 is interbundling and it is thicker than CE3.

Strain Variation. To explore the Young's modulus effect on elastic stability of CE, we developed a contact model to simulate bending CNC CE in a finite element method. In the contact model, normal pressure and tangential friction force can be transferred via the interface between CNC layer and substrate. Two CNC CEs of CE−M1 and CE−M2 are modeled. The E_Y values of the two CEs are set the same. The E_X values of CE−M1 and CE−M2 are set of 1×10^3 and 1×10^7 Pa, respectively. The huge difference of E_X values is for a clear reflection of its effect.

With the same vertical displacement load of 2 mm, the simulation results for CE−M1 and CE−M2 are shown in panels a and b in Figure 7, respectively. The upper or lower part shows the CE at upward or downward bended status, respectively. The contour variation of elastic strain intensity and deformation are observed. With bigger E_X value, the CE−M2 is delamination compared to CE−M1. The region with bigger strain indicates the material there is more likely to peel or crack, especially when the material is in a weak porous structure.[33] Compared to CE−M2, the CE−M1 shows bigger strain at either upward or downward status although it is not delamination. These indicate the CNC on CE−M1 is more likely to peel (or crack). The CNC strain on CE−M2 is much smaller. This can be attributed to the delamination failure, which releases the strain.[23] These simulation results indicate the failure mode of CNC layer switches from peeling (or cracking) to delamination with increasing Young's modulus and
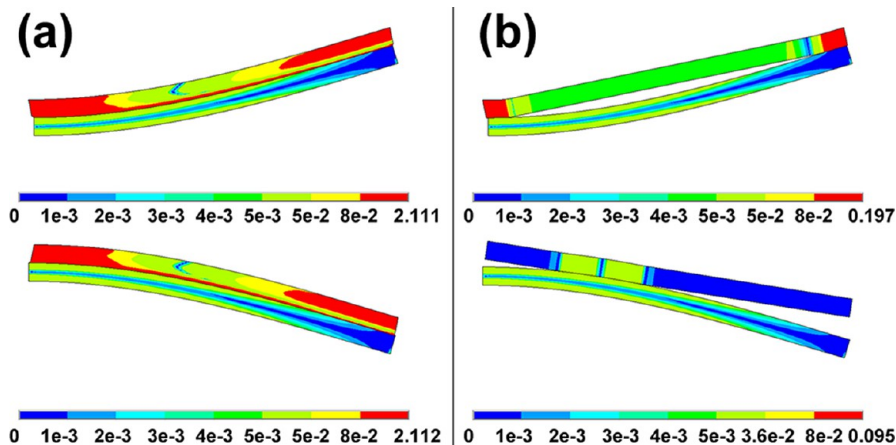

Figure 7. Simulation results for (a) CE−M1 and (b) CE−M2. The upper or lower part shows the CE at upward or downward bended status, respectively.

unchanged thickness of CNC layer. In literature, experimental results indicate that the fracture failure stress increases with increasing Young's modulus when the samples have the same thicknesses,[34] and larger interfacial stresses has potential to arouse delamination.[35,36] These results further verify the simulation results obtained above. Therefore, the CNC E_X of CE3 (or CE4) is deduced to be larger than that for CE2. The larger E_X value can be attributed to bigger horizontal interbundling degree for CE3 (or CE4). Similar results are deduced in literatures.[37] In the literature, the Young's modulus of nanofilms is demonstrated to be strongly influenced by its nanostructure.[38]

Although the CE2 and CE1 have similar CNC thicknesses, the CNC on CE2 only crack compared to the CNC peeling on CE1. This indicates the CNC E_X (or interbundling degree) of CE2 is bigger than that of CE1. In general, a larger horizontal interbundling degree (or bigger E_X value) can prevent peeling (or cracking), although it will bring detachment.

Environment Effect. The vibration test is carried out in a lab environment. To study the environment effect on the CE behavior, we checked the CE behaviors by EIS and Tafel measures as a function of CE exposed time in lab environment. The needed time for five continuous vibration sections is less than 6 h, as mentioned above. Then, the measures are carried out after the CEs are exposed for 0, 2, 4, and 6 h.

The Ohm series resistance (R_S), charge-transfer resistance at CE/electrolyte interface (R_{CT}), constant phase element (CPE), and Warburg element (Z_N) are obtained by EIS measurement. The exchange current density (J_0) is obtained by Tafel polarization measurement. The R_{CT} and J_0 values reflect the catalytic ability of CE. Here, the catalytic ability is defined as the total reduction ability for a CE converting I_3^- to I^-. The R_{SUM} is calculated by $R_{SUM} = R_S + R_{CT} + Z_N$.[39,40] It is an important parameter to reflect electrical conductivity of CE.

The Nyquist plots for these CEs when the CEs are not exposed in air are shown in Figure 8a, and their equivalent circuit is shown in the inset. These equivalent parameters are fitted by Zview software, and the values are for a single CE in a dummy cell. The Tafel curves are shown in Figure 8b. These equivalent parameters and J_0 values are listed in Table 2. Among these CEs, the CE2 shows the smallest R_{CT} and R_{SUM} values, indicating the highest catalytic ability and electrical conductivity.[24,41,42] Its highest catalytic ability is further demonstrated by its biggest J_0 value.

The R_S, R_{CT}, J_0, and R_{SUM} variations are shown in Figure 9a–d, respectively. For each parameter, the measured values are normalized by its initial values as listed in Table 2. It is observed all parameters just appear slight variations when the exposed time exceeds 2 h, which can be attributed to the moisture effect in air.[43−45] In Figure 9c, the variation trend of J_0 value for each CE is invert to that of R_{CT} value, because the J_0 generally shows an inverse relationship with corresponding R_{CT} value.[24,41] For all parameters, the variations for CE1 or CE2 are relatively more remarkable compared to those for CE3 or CE4, which is probably because their porous CNC structures can absorb more moisture in air.[46] To evaluate the environment effect extent on CE behavior, we need to compare these parameter variations to those aroused in vibration test. This comparison and environment effect evaluation will be discussed in the following section.

Electrochemical Parameter Variation. To explore the vibration effect on electrical and catalytic properties of CE, the EIS and Tafel polarization curves of these CEs are measured
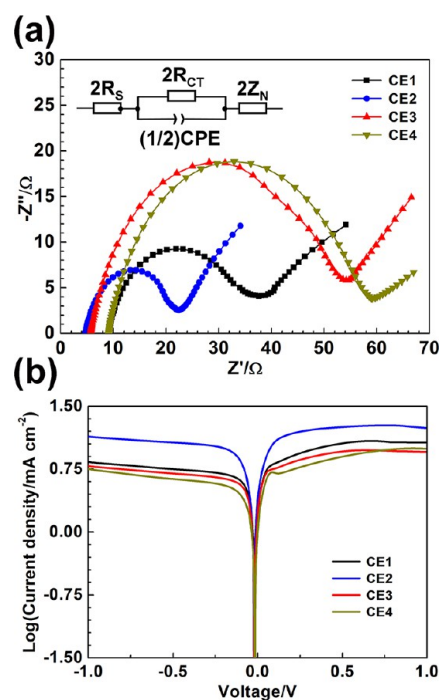

Figure 8. (a) Nyquist plots for CEs. The inset is the equivalent circuit. (b) Tafel polarization curves for CEs.

with increasing vibration cycles. With increasing vibration cycles, the variation curves of R_S, R_{CT}, J_0, and R_{SUM} values are shown in Figure 10a–d, respectively. For each parameter, the measured values are normalized by its initial values as listed in Table 2. They all significantly vary in the beginning, and then tend to stabilize. Here, steeper curve indicates weaker stability. In Figure 10a, the R_S values of CE1 and CE2 decreases with increasing vibration cycle. These can be attributed to the peeling−off for CE1 (Figure 5e) and the crack failure for CE2 (Figure 5f). These failures mean the quantity reduction of CNTs on substrate, which directly shortens the transfer path of electron in CNC layer. In contrast, the R_S values of CE3 and CE4 increase. These can be attributed to the increase of interface impedance between the CNC layer and substrate affected by the delamination (Figure 5g, h). In general, the order of R_S stability is CE1≈ CE2 ≈ CE3 > CE4.

In Figure 10b, the R_{CT} values of CE1 and CE2 increase with increasing vibration cycle. These can also be attributed to their peeling and crack failures, which directly reduce the real surface area of CNTs and then bring down the catalytic ability of CE.[24] The R_{CT} values of CE3 and CE4 almost remain invariant. These reveal the delamination plays a weak effect on catalytic ability, which can attributed to the invariable quantity of CNC on substrate.[24] In general, the order of R_{CT} stability is CE3 > CE4 > CE2 > CE1. The order of J_0 stability is the same to R_{CT} value, as shown in Figure 10c, because the J_0 value generally has an inverse relationship to corresponding R_{CT} value.[24,41] These further demonstrate the effects of failure modes on catalytic ability of CE as discussed above. Here, the J_0 value of CE3 increases weakly. This is maybe because the vibration looses the CNC layer then makes its real surface area increase.

The R_{SUM} value is an important parameter, which plays remarkable effect on the performance of DSSCs.[24,40] In Figure 10d, the order of R_{SUM} stability is the same as the R_{CT} value, indicating the R_{CT} stability give main effect on R_{SUM} stability. The effect from R_S can be ignored because it is so weak.

Table 2. Fitted Equivalent Resistances and Exchange Current Density J_0 Values[a]

CE	R_S (Ω)	R_{CT} (Ω)	Z_N (Ω)	R_{SUM} (Ω)	J_0 (mA cm^{-2})
CE1	4.6 ± 0.2	14.5 ± 0.2	20.2 ± 0.2	39.3 ± 0.4	3.0 ± 0.1
CE2	2.3 ± 0.1	9.0 ± 0.2	25.8 ± 0.2	37.1 ± 0.3	4.0 ± 0.1
CE3	2.9 ± 0.1	24.5 ± 0.2	37.3 ± 0.3	64.7 ± 0.4	2.7 ± 0.1
CE4	4.6 ± 0.2	25.0 ± 0.1	34.5 ± 0.3	64.1 ± 0.4	1.8 ± 0.1

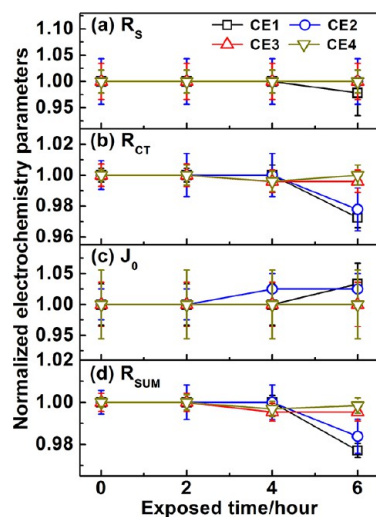[a]The results with standard error are obtained from five samples.

Figure 9. Variations in (a) R_S, (b) R_{CT}, (c) J_0 and (d) R_{SUM} values of vibration−free CEs with increasing exposed time in lab environment.
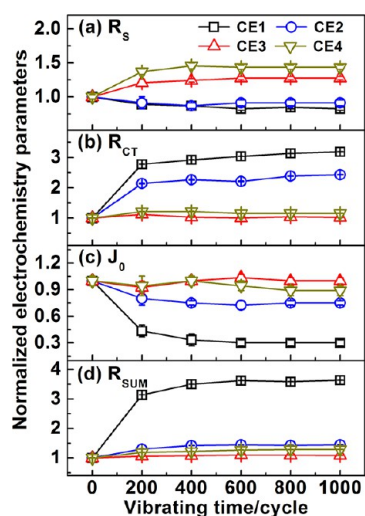

Figure 10. Variations in (a) R_S, (b) R_{CT}, (c) J_0, and (d) R_{SUM} values with increasing vibration cycles.

Although a larger interbundling degree will bring delamination, it can prevent peeling or cracking and then stabilize the R_{CT} value. Therefore, bigger interbundling degree of CNC is beneficial to R_{SUM} stability. The CE3 shows the highest R_{SUM} stability, which can be attributed to its larger interbundling degree and smallest thickness of the CNC layer.

For R_S, R_{CT}, J_0 and R_{SUM} values, compared to their variation amplitude affected by vibration shown in Figure 10, those affected by environment as shown in Figure 9 are relatively less. Therefore, the environment effect on CE behavior can be ignored in the vibration test.

DSSC Performance Variation. To estimate the elastic stabilities of these CEs, we studied the performance parameter variations of these CE-based DSSCs with increasing vibration cycles. These parameters consist of open circuit voltage (V_{OC}), short current density (J_{SC}), fill factor (FF), and PCE. Before the CEs are exposed and vibrated, the cell parameters are listed in Table 3. The related $J-V$ curves are shown in Figure 11. A

Table 3. Performance Parameters of DSSCs[a]

CE	V_{OC} (V)	J_{SC} (mA cm^{-2})	FF	PCE (%)
CE1	0.76 ± 0.03	10.7 ± 0.3	0.71 ± 0.03	5.8 ± 0.4
CE2	0.76 ± 0.02	10.8 ± 0.2	0.72 ± 0.02	5.9 ± 0.3
CE3	0.73 ± 0.02	11.1 ± 0.2	0.71 ± 0.01	5.8 ± 0.3
CE4	0.73 ± 0.01	11.1 ± 0.2	0.62 ± 0.02	5.0 ± 0.2

[a]The results with standard error are obtained from five samples.
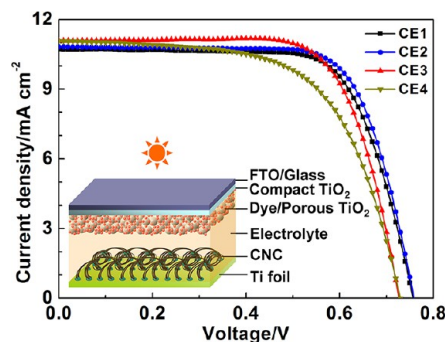

Figure 11. $J-V$ curves for DSSCs. The inset is an assembling schematic for a DSSC with a CNC CE.

schematic of an assembling cell with a CNC CE is shown in the inset. The PCE order for these cell is CE2 > CE1 = CE3 > CE4. A smaller R_{SUM} value is demonstrated beneficial to cell performance. It can bring a smaller IR drop and then to improve the cell V_{OC} value,[47] a smoother charge transport in cell and then to improve the J_{SC} value,[48] and a larger FF value.[40,48,49] For these CEs, the R_{SUM} order is CE3 > CE4 > CE1 > CE2, as shown in Table 2, which can explain the PCE order of CE2 > CE1 > CE4, as shown in Table 3. However, the PCE of CE3-based cell is not suitable for this regularity. The J_{SC} of the CE3-based cell is observed to be the maximum value among these cells, which probably comes from the solid−solid interface in its carbon-based materials on CE.[42,50,51] This interface can promote electron transport by acting as a fast passageway between the substrate and functional layer and then improve the cell J_{SC} value.[24] Therefore, the PCE of CE3-based cell is relatively high, although the CNC on CE3 is much thinner than those on other CEs.

The variation curves of these parameters with increasing vibration cycles are shown in Figure 12. For each parameter, the measured values are normalized by their initial values as listed in Table 3. In Figure 12a, all V_{OC} values decrease with
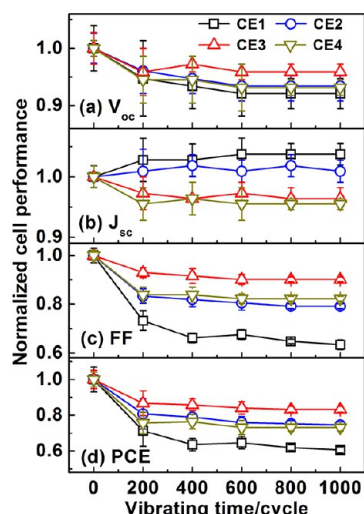
Figure 12. Variations in (a) V_{OC}, (b) J_{SC}, (c) FF, and (d) PCE for DSSCs with increasing vibration cycles.

increasing vibration cycles. The order of V_{OC} stability is CE3 > CE4 ≈ CE2 > CE1, generally according to that of R_{SUM} value, because bigger R_{SUM} can bring larger IR drop.[24,47] In Figure 12b, the J_{SC} values of CE1 and CE2 increase and those of CE3 and CE4 decrease. These variation trends are opposite to corresponding R_S values. The J_{SC} stabilities for these cells are close. These indicate that the R_S stability has a weak effect on J_{SC} stability, although the R_S inversely affects the J_{SC} value. In Figure 12c, the FF values all decrease with increasing vibration cycles. Compared to the V_{OC} and J_{SC} values, the FF shows the biggest variation degree. Its stability order is the same as R_{SUM}, because the R_{SUM} can seriously affect the FF value.[48,49] In Figure 12d, the resulting PCE shows a stability order of CE3 > CE2 > CE4 > CE1, which is close to FF value. The PCE stability of CE2 is higher than CE4, which can be attributed to the increasing J_{SC} value of CE2 compared to decreasing J_{SC} value of CE4, as discussed above. In general, the R_{SUM} stability directly determines the PCE stability by its dominant effects on V_{OC} and FF stabilities. By contrast, the R_S only weakly affects PCE stability. After five vibration sections, the R_{SUM} of CE3 varies less than 10%, which leads the PCE of CE3-based cell to remain at 80% of the initial value, indicating that the CE3 own the highest stability.

Potential Application. Herein, for Ti-foil-supported porous CNC electrode, the structure parameters of CNC thickness and CNC interbundling degree (Young's modulus) are demonstrated as two important factors on the elastic stability of electrode. This studied electrode belongs to a type of double-layer electrode, where the lower substrate is an elastic supporter for generating elastic vibration, and upper layer is for a special function. In a general double-layer electrode, the forementioned two structure parameters still exist for upper functional layer, so the results deduced here have the potential to be applied for the elastic stability study in this type of electrode. In addition, there is another type of elastic electrode, that of a self-supported single film. The film simultaneously acts as elastic supporter and functional layer. In the literature, these self-supported single-film electrodes consist of carbon aerogels,[6] ZnO/ployer composite,[52] and Al_2O_3−NiAl composites.[53] When the failure appears in a single-layer electrode, the single layer can be divided into two layers, consisting of one failure layer and another not-failure layer. This resulting structure is similar to that of double-layer electrode. Therefore, the deduced results here can provide a reference for the elastic stability study for the single-layer electrode.

5. CONCLUSIONS

An out-of-plane vibration test method is carried out to directly study the elastic stability of CNC CE for DSSCs. The CNC, hybridized with CNTs and Ni nanoparticles, is fabricated on an elastic Ti substrate. The elastic stability of CE is estimated by that of the CE-based DSSC PCE. The stability is analyzed from the views of the CNC morphologies, R_S, R_{CT}, J_0, and R_{SUM} values of CEs. Their effects on V_{OC}, J_{SC}, FF, and PCE are discussed. Furthermore, elastic strain and deformation are studied by a contact model in a finite element method. The results suggest that the R_{SUM} stability can reflect the CE stability. A thinner thickness and bigger interbundling degree of CNC layer benefit the elastic stability of CE. Although a large interbundling degree can bring delamination, it prevents peeling and cracking failures and then stabilizes the R_{SUM} value. With the optimized CNC layer, the R_{SUM} value varies less than 10% and PCE of the CE-based DSSC can remain at 80% of the initial value, even if the CE is springed 1000 times with the maximum amplification of about 10 mm. The test method is interesting and the results have potential use for stability study of general elastic devices.

■ AUTHOR INFORMATION

Corresponding Author

*E-mail: gjfang@whu.edu.cn.

Notes

The authors declare no competing financial interest.

■ REFERENCES

(1) Duerloo, K.-A. N.; Ong, M. T.; Reed, E. J. *J. Phys. Chem. Lett.* **2012**, *3*, 2871−2876.

(2) Dobrzynska, J. A.; Gijs, M. A. M. *J. Micromech. Microeng.* **2013**, *23*, 015009.

(3) Jin, Z. H. *Int. J. Fract.* **2013**, *180*, 129−136.

(4) Rogers, J. A.; Someya, T.; Huang, Y. *Science* **2010**, *327*, 1603−1607.

(5) Zhang, C. J.; Pang, S. P.; Kong, Q. S.; Liu, Z. H.; Hu, H.; Jiang, W.; Han, P. X.; Wang, D.; Cui, G. L. *RSC Adv.* **2013**, *3*, 1336−1340.

(6) Sun, H.; Xu, Z.; Gao, C. *Adv. Mater.* **2013**, *25*, 2554−2560.

(7) Kerman, K.; Tallinen, T.; Ramanathan, S.; Mahadevan, L. *J. Power Sources* **2013**, *222*, 359−366.

(8) Liang, J. F.; Zhao, Y.; Guo, L.; Li, L. D. *ACS Appl. Mater. Interface* **2012**, *4*, 5742−5748.

(9) Ettema, G. J. C. *Eur. J. Appl. Physiol.* **2001**, *85*, 457−465.

(10) Barois, T.; Ayari, A.; Vincent, P.; Perisanu, S.; Poncharal, P.; Purcell, S. T. *Nano Lett.* **2013**, *13*, 1451−1456.

(11) Lou, F.; Zhou, H.; Huang, F.; Vullum-Bruer, F.; Tran, T. D.; Chen, D. *J. Mater. Chem. A* **2013**, *1*, 3757−3767.

(12) Li, Y.; Lee, D.-K.; Kim, J. Y.; Kim, B.; Park, N.-G.; Kim, K.; Shin, J.-H.; Choi, I.-S.; Ko, M. J. *Energy Environ. Sci.* **2012**, *5*, 8950.

(13) Li, Y.; Yoo, K.; Lee, D.-K.; Kim, J. H.; Park, N.-G.; Kim, K.; Ko, M. J. *Curr. Appl. Phys.* **2010**, *10*, e171−e175.

(14) Ye, S.; Feng, J.; Wu, P. *J. Mater. Chem. A* **2013**, *1*, 3495−3502.

(15) Hyun, D. C.; Park, M.; Park, C.; Kim, B.; Xia, Y.; Hur, J. H.; Kim, J. M.; Park, J. J.; Jeong, U. *Adv. Mater.* **2011**, *23*, 2946−2950.

(16) Yu, Z.; Zhang, Q.; Li, L.; Chen, Q.; Niu, X.; Liu, J.; Pei, Q. *Adv. Mater.* **2011**, *23*, 664−668.

(17) Botelho, E. C.; Pardini, L. C.; Rezende, M. C. *J. Appl. Polym. Sci.* **2007**, *106*, 3143−3148.

(18) Wang, X. L.; Li, T. J.; Adam, J.; Yang, J. *J. Mater. Chem. A* **2013**, *1*, 3580−3586.

(19) Xu, H.; Komvopoulos, K. *Int. J. Solids Struct.* **2013**, *50*, 876−886.

(20) Vasques, C. M. A. *Smart Mater. Struct.* **2012**, *21*, 125003.

(21) Xiang, H. J.; Yang, J. *Compos., Part B* **2008**, *39*, 292−303.

(22) Komijani, M.; Kiani, Y.; Esfahani, S. E.; Eslami, M. R. *Compos. Struct.* **2013**, *98*, 143−152.

(23) Park, S.-I.; Ahn, J.-H.; Feng, X.; Wang, S.; Huang, Y.; Rogers, J. A. *Adv. Funct. Mater.* **2008**, *18*, 2673−2684.

(24) Zeng, W.; Fang, G.; Wang, X.; Zheng, Q.; Li, B.; Huang, H.; Tao, H.; Liu, N.; Xie, W.; Zhao, X.; Zou, D. *J. Power Sources* **2013**, *229*, 102−111.

(25) Liu, N.; Fang, G.; Yang, X.; Zeng, W.; Li, C.; Wang, M.; Li, J.; Zhao, X. *Diamond Relat. Mater.* **2009**, *18*, 1375−1380.

(26) Tai, Q. D.; Chen, B. L.; Guo, F.; Xu, S.; Hu, H.; Sebo, B.; Zhao, X. Z. *ACS Nano* **2011**, *5*, 3795−3799.

(27) Liu, Y. L.; Fu, Q.; Pan, C. X. *Carbon* **2005**, *43*, 2264−2271.

(28) Yuan, L.; Saito, K.; Pan, C.; Williams, F. A.; Gordon, A. S. *Chem. Phys. Lett.* **2001**, *340*, 237−241.

(29) Bakshi, S. R.; Lahiri, D.; Agarwal, A. *Int. Mater. Rev.* **2010**, *55*, 41−64.

(30) Han, Y. D.; Nai, S. M. L.; Jing, H. Y.; Xu, L. Y.; Tan, C. M.; Wei, J. *J. Mater. Sci.: Mater. Electron.* **2011**, *22*, 315−322.

(31) Wang, X.; Krommenhoek, P. J.; Bradford, P. D.; Gong, B.; Tracy, J. B.; Parsons, G. N.; Luo, T. J. M.; Zhu, Y. T. *ACS Appl. Mater. Interfaces* **2011**, *3*, 4180−4184.

(32) Xu, M.; Futaba, D. N.; Yumura, M.; Hata, K. *ACS Nano* **2012**, *6*, 5837−5844.

(33) Simone, A. E.; Gibson, L. J. *Acta Mater.* **1996**, *44*, 1437−1447.

(34) Schwingel, D.; Taylor, R.; Haubold, T.; Wigren, J.; Gualco, C. *Surf. Coat. Technol.* **1998**, *108−109*, 99−106.

(35) Podczeck, F.; Al-Muti, E. *Eur. J. Pharm. Sci.* **2010**, *41*, 483−488.

(36) Cao, H. C.; Evans, A. G. *Acta Metall. Mater.* **1991**, *39*, 2997−3005.

(37) Bailey, S.; Mays, E.; Michalak, D. J.; Chebiam, R.; King, S.; Sooryakumar, R. *J. Phys. D: Appl. Phys.* **2013**, *46*, 045308.

(38) Shaoli, F.; Mei, Z.; Anvar, A. Z.; Ray, H. B. *J. Phys.: Condens. Mater.* **2010**, *22*, 334221.

(39) Ramasamy, E.; Lee, W. J.; Lee, D. Y.; Song, J. S. *Electrochem. Commun.* **2008**, *10*, 1087−1089.

(40) Wang, Q.; Ito, S.; Gratzel, M.; Fabregat-Santiago, F.; Mora-Sero, I.; Bisquert, J.; Bessho, T.; Imai, H. *J. Phys. Chem. B* **2006**, *110*, 25210−25221.

(41) Wu, M.; Lin, X.; Wang, Y.; Wang, L.; Guo, W.; Qi, D.; Peng, X.; Hagfeldt, A.; Grätzel, M.; Ma, T. *J. Am. Chem. Soc.* **2012**, *134*, 3419−3428.

(42) Huang, S.; Sun, H.; Huang, X.; Zhang, Q.; Li, D.; Luo, Y.; Meng, Q. *Nanoscale Res. Lett.* **2012**, *7*, 222.

(43) Mikoshiba, S.; Murai, S.; Sumino, H.; Kado, T.; Kosugi, D.; Hayase, S. *Curr. Appl. Phys.* **2005**, *5*, 152−158.

(44) Zhu, K.; Jang, S.-R.; Frank, A. J. *Energy Environ. Sci.* **2012**, *5*, 9492−9495.

(45) Zahab, A.; Spina, L.; Poncharal, P.; Marliere, C. *Phys. Rev. B* **2000**, *62*, 10000−10003.

(46) Horikawa, T.; Sakao, N.; Hayashi, J.; Do, D. D.; Katoh, M.; Sotowa, K. I. *Adsorpt. Sci. Technol.* **2013**, *31*, 135−144.

(47) Imoto, K.; Takahashi, K.; Yamaguchi, T.; Komura, T.; Nakamura, J.-i.; Murata, K. *Sol. Energy Mater. Solar Cells* **2003**, *79*, 459−469.

(48) Jia, R.; Chen, J.; Zhao, J.; Zheng, J.; Song, C.; Li, L.; Zhu, Z. *J. Mater. Chem.* **2010**, *20*, 10829−10834.

(49) Mane, R. S.; Lee, W.-J.; Lokhande, C. D.; Cho, B. W.; Han, S.-H. *Curr. Appl. Phys.* **2008**, *8*, 549−553.

(50) Murakami, T. N.; Ito, S.; Wang, Q.; Nazeeruddin, M. K.; Bessho, T.; Cesar, I.; Liska, P.; Humphry-Baker, R.; Comte, P.; Pechy, P.; Gratzel, M. *J. Electrochem. Soc.* **2006**, *153*, A2255−A2261.

(51) Seo, S. H.; Kim, S. Y.; Koo, B.-K.; Cha, S.-I.; Lee, D. Y. *Langmuir* **2010**, *26*, 10341−10346.

(52) Devi, R. R.; Maji, T. K. *Ind. Eng. Chem. Res.* **2012**, *51*, 3870−3880.

(53) Song, J.; Hu, W.; Gottstein, G. *Mater. Sci. Eng., A* **2011**, *528*, 7790−7800.